Experimental and Computational Multiphase Flow
Vol. 8, No. 2, 2026, 295–312
https://doi.org/10.1007/s42757-025-0267-9

Transport and deposition of pharmaceutical aerosols in a helium–oxygen mixture in a CT-based nose-to-lung respiratory tract

Xinlei Huang[1], Akshoy Ranjan Paul[2], Prashanta Kumar Mandal[3], Suvash C. Saha[1] (✉)

1. *School of Mechanical and Mechatronic Engineering, Faculty of Engineering and Information Technology, University of Technology Sydney, Sydney, NSW 2007, Australia*
2. *Department of Applied Mechanics, Motilal Nehru National Institute of Technology Allahabad, Prayagraj 211004, India*
3. *Department of Mathematics, Visva-Bharati, Santiniketan 731 235, WB, India*

Abstract

Helium–oxygen mixtures (HeliOx) have been proposed to enhance aerosol drug delivery by reducing airflow turbulence and facilitating deeper penetration of medications into the respiratory tract. However, previous studies on HeliOx efficacy have yielded mixed results, often limited by unrealistic anatomical models and steady-state assumptions, and focus on restricted sections of the airway. This study aims to address these limitations by investigating the transport and deposition of pharmaceutical aerosols in HeliOx compared to atmospheric air using a realistic, computed tomography-based nose-to-lung respiratory tract model that extends from a face mask to the 13th generation of tracheobronchial airways. Experimentally measured, dynamic breathing profiles were incorporated to simulate realistic inhalation conditions. Pharmaceutical aerosols with diameters ranging from 1 to 100 μm were released under two conditions: ambient air and HeliOx. Computational fluid–particle dynamics simulations were performed to model and visualize the transport and deposition patterns of aerosols throughout the respiratory tract during inhalation. The simulation results indicate that HeliOx promotes more steady airflow with reduced turbulence, facilitating a deeper delivery of drug aerosols compared to ambient air. Specifically, HeliOx reduced turbulence intensity in the nasal cavity, larynx, and upper trachea regions, and enhanced aerosol penetration to the lower respiratory tract, increasing the deposition fraction in the deeper lung regions. These findings suggest that utilizing HeliOx as a carrier gas can improve deep lung-targeted drug delivery, potentially enhancing therapeutic outcomes for pulmonary diseases.

Keywords

pharmaceutical aerosol
computational fluid–particle dynamics
particle-laden flow
targeted delivery
human respiratory tract
health

Article History

Received: 31 December 2024
Revised: 16 April 2025
Accepted: 13 June 2025

Research Article

© The Author(s) 2026

1 Introduction

Since its initial use in 1935 (Barach, 1935), helium has been employed to improve airflow in obstructed airways (Curtis et al., 1986; Despas et al., 1972; Ingram Jr. and McFadden Jr., 1977; Kass and Castriotta, 1995; Lu et al., 1976; Skrinskas et al., 1983). Extensive empirical and theoretical research has substantiated the advantages of using a helium–oxygen mixture (HeliOx) for treating asthma and chronic obstructive pulmonary disease (D'Angelo et al., 2009; Kass and Castriotta, 1995; Pecchiari et al., 2004), as well as for enhancing respiratory support (Del Puppo et al., 2023). Notably, HeliOx is a noncarcinogenic and nontoxic gas with no long-term effects on human organs (Harris and Barnes, 2008; Hashemian and Fallahian, 2014). A critical property of HeliOx is its viscosity—similar to that of atmospheric air—combined with a density nearly six times lower, which reduces turbulence effects and can increase flow rates by up to 50% (Hashemian and Fallahian, 2014). This characteristic makes it desirable for targeted drug delivery therapy, as less turbulent flow with higher velocity generally facilitates the delivery of aerosolized medications to the deeper regions of the respiratory tract (Corcoran and Gamard, 2004; Abd-Elsayed and McMaster, 2023). Therefore, the focus of this study is to

✉ Suvash.Saha@uts.edu.au

Nomenclature

a_{1D}, a_{2D}, a_{3D}	adjustable parameters for Eq. (13)
A_p	projected particle surface area (m^2)
C_ω	rotational drag coefficient
d_p	aerosol diameter (m)
F	force vector (N)
F_2	blending function for Eq. (5)
g	gravitational acceleration, which equals to 9.81 ($m \cdot s^{-2}$)
I_p	moment of inertia of aerosol ($kg \cdot m^2$)
k	turbulence kinetic energy ($m^2 \cdot s^{-2}$)
p	static pressure (Pa)
t	time (s)
u	fluid velocity vector ($m \cdot s^{-1}$)
u_p	aerosol velocity ($m \cdot s^{-1}$)
G_b	turbulence generation due to buoyancy
$G_{\omega b}$	turbulence generation due to buoyancy for ω equation
P_k	rate of production of turbulent kinetic energy (s^{-1})
Pr_t	turbulent Prandtl number
P_ω	rate of production of specific dissipation rate (s^{-1})
Re	relative Reynolds number
S	strain rate magnitude (s^{-1})
S_{ij}	mean component of the rate of deformation s_{ij}
T_p	torque applied to an aerosol ($N \cdot m$)
x_i, x_j	Cartesian coordinate
y	distance to the next surface (m)
Y_k	dissipation of turbulent kinetic energy due to turbulence
Y_ω	dissipation of specific dissipation rate due to turbulence

Greek symbols

α	model constant, which is equal to 0.44
α^*	damping coefficient
σ_k	turbulent Prandtl number for turbulent kinetic energy
σ_ω	turbulent Prandtl number for the specific dissipation rate
μ	molecular viscosity ($N \cdot s \cdot m^{-2}$)
μ_t	turbulent viscosity ($N \cdot s \cdot m^{-2}$)
ν	kinematic viscosity ($m^2 \cdot s^{-1}$)
ρ	fluid density ($kg \cdot m^{-3}$)
ρ_p	aerosol density ($kg \cdot m^{-3}$)
$\bar{\bar{\tau}}$	stress tensor (Pa)
τ_r	relaxation time
ω	specific dissipation rate (s^{-1})

explore how the variations in deposition fractions between HeliOx and atmospheric air can be utilized to optimize drug delivery in the human respiratory tract.

Despite the complexity of the human respiratory system and the inherent risks associated with *in vivo* interventions, there remains an urgent demand for comprehensive research in this domain, particularly concerning the targeted administration of aerosolized medications (Dhand and Guntur, 2008; Kleinstreuer et al., 2014; Labiris and Dolovich, 2003; Tian et al., 2014). Experimental investigations have yielded mixed results regarding the efficacy of HeliOx in aerosol delivery. Darquenne and Prisk (2004) measured aerosol deposition in the respiratory tracts of healthy subjects inhaling monodisperse particles using both air and an 80% helium and 20% oxygen (80/20) HeliOx mixture at a constant flow rate and tidal volume of 900 mL. They found a small but statistically significant decrease in total deposition with HeliOx for 1 and 2 μm particles. The findings imply that HeliOx may reduce deposition in the upper airways and enhance delivery to the small airways and alveoli.

In pediatric models, Corcoran et al. (2003) evaluated methods to increase nebulized drug delivery to the lungs using an MRI-based airway model of a 5-year-old child. They compared four methods: standard nebulization with air, nebulization with 70/30 HeliOx, and both methods augmented with an aerosol-conserving reservoir. Their results demonstrated that HeliOx increased pulmonary drug delivery by 50% compared to air, and the combination of HeliOx with a reservoir led to an 82% increase. The enhanced delivery with HeliOx was attributed to decreased deposition within the nebulizer and delivery apparatus, highlighting its potential to improve pediatric aerosol therapy.

Conversely, Dailey et al. (2017) assessed aerosol delivery through an adult high-flow nasal cannula (HFNC) using 80/20 HeliOx and 100% oxygen. Employing a vibrating mesh nebulizer and simulating both quiet and distressed adult breathing patterns, they investigated the inhaled dose of albuterol sulfate at three constant flow rates (10, 30, and 50 L/min). Their findings indicated that, for quiet breathing, increasing flow rates with both gases significantly decreased the percentage of inhaled doses. Under distressed breathing conditions, higher flow rates improved aerosol delivery, but there was no significant difference between HeliOx and oxygen. The study concluded that HeliOx did not significantly enhance aerosol delivery via HFNC under the tested conditions.

Over the past two decades, the application of computational

fluid dynamics (CFD) has expanded drastically (Huang et al., 2022), fundamentally enhancing our understanding of physiological phenomena in both healthy and pathological conditions (Saha et al., 2024a). While numerous numerical investigations have explored pharmaceutical aerosol transport and deposition in the nasal cavity (Dong et al., 2018; Rygg et al., 2016; Rygg and Longest, 2016), oropharyngeal cavity (Dastoorian et al., 2022; Vara Almirall et al., 2022; Xi et al., 2016), and tracheobronchial airways (Cheng, 2014; Khajeh-Hosseini-Dalasm and Longest, 2015; Tian et al., 2011), there is a notable lack of research on HeliOx-assisted targeted aerosol delivery. Gemci et al. (2003) conducted a numerical analysis of aerosol deposition in the larynx and trachea using monodisperse aerosols in both air and a 70/30 HeliOx mixture. Utilizing the KIVA-3 V software at a flow rate representative of adult breathing (18 L/min), they found that the flow structures in HeliOx and air were highly similar, with differences in turbulent kinetic energy and velocity magnitude typically less than 5%. This suggests that under the conditions studied, HeliOx may not significantly alter upper airway flow dynamics compared to air.

In contrast, other CFD studies have reported notable differences when using HeliOx. Farooq et al. (2023) developed a mixture model to understand the impact of 78/22 HeliOx and a HeliOx–air mixture on flow behavior and particle transport in both idealized and age-specific upper airways. Their simulations indicated that HeliOx reduced turbulence intensity in the extrathoracic region, resulting in lower deposition efficiencies in the third- to fifth-generation (G3–G5) lung airways compared to air and the HeliOx–air mixture. Similarly, Islam et al. (2020) employed CFD simulations on CT-based upper airway geometries to investigate aerosol particle transport using an 80/20 HeliOx mixture. They observed that HeliOx breathing reduced turbulence intensity and deposition efficiency in the upper airways relative to air breathing. Both studies suggest that HeliOx can decrease unwanted aerosol deposition in the upper airways, potentially enhancing targeted drug delivery to deeper lung regions.

A review of the literature reveals several knowledge gaps. First, many studies have employed unrealistic geometries that lack the anatomical details present in the human pulmonary system. These anatomical features have been shown to greatly influence local airflow and particle deposition patterns (Huang et al., 2025b). Second, prior studies often assume constant boundary conditions or adopt steady-state conditions. In reality, a breathing profile with changing velocity reflects tidal volume variations and has a significant impact on particle dynamics (Wedel et al., 2022). Finally, most research focuses on a limited section of the respiratory tract, such as the larynx in Gemci et al. (2003) or the four generations of tracheobronchial airways in Islam et al. (2020). A more comprehensive model of the respiratory tract could provide a complete view of how aerosols are transported and deposited throughout the airway.

Therefore, the present study aims to address these gaps by applying a realistic, CT-based model of the respiratory tract—from a face mask to the 13th generation tracheobronchial airways—incorporating experimentally measured, changing breathing profiles. Pharmaceutical aerosols with diameters ranging from 1 to 100 μm were released under two conditions: ambient air and HeliOx. For the first time, the transport and deposition patterns of aerosols from their release in a facial mask are modeled and visualized. This comprehensive analysis of different inhalation conditions could assist medical experts in optimizing targeted drug delivery and improving the treatment of pulmonary diseases.

2 Methodology

2.1 Computational model of the respiratory tract

This study presents the development of a comprehensive computational model of the human respiratory tract, employing advanced methodologies for high-precision modeling and simulation. The process began with the segmentation of detailed three-dimensional surface models from CT images utilizing Mimics Medical 21 (Medical, 2021). Subsequent enhancements and sectioning were performed using Geomagic Wrap 2021 (GeomagicWrap, 2022), and the refined model underwent further postprocessing in Siemens NX 12 (Siemens, 2017) to enhance detail and fidelity. This model was then imported into Ansys (ANSYS, 2020a) for mesh generation and simulation tasks, building upon techniques outlined in our previous publication (Huang et al., 2025a, 2025b).

The finalized model, depicted in Fig. 1(a), includes detailed representations of the nasal cavity, nasopharynx, oral cavity, oropharynx, larynx, laryngopharynx, and airways from the trachea to the 13th generation of branching. For simulation efficiency, anatomical features were strategically simplified into several regions, enabling more focused meshing and computational analysis. Ethical clearance for the use of human CT scans was obtained from the Human Research Ethics Committee of the University of Technology Sydney, with approval reference ETH23-8670 issued on September 7, 2023.

2.2 Governing equations for the fluid

This study applies the continuity and momentum equations to model the aerodynamics within the human respiratory tract, employing the k–ω shear stress transport (SST)

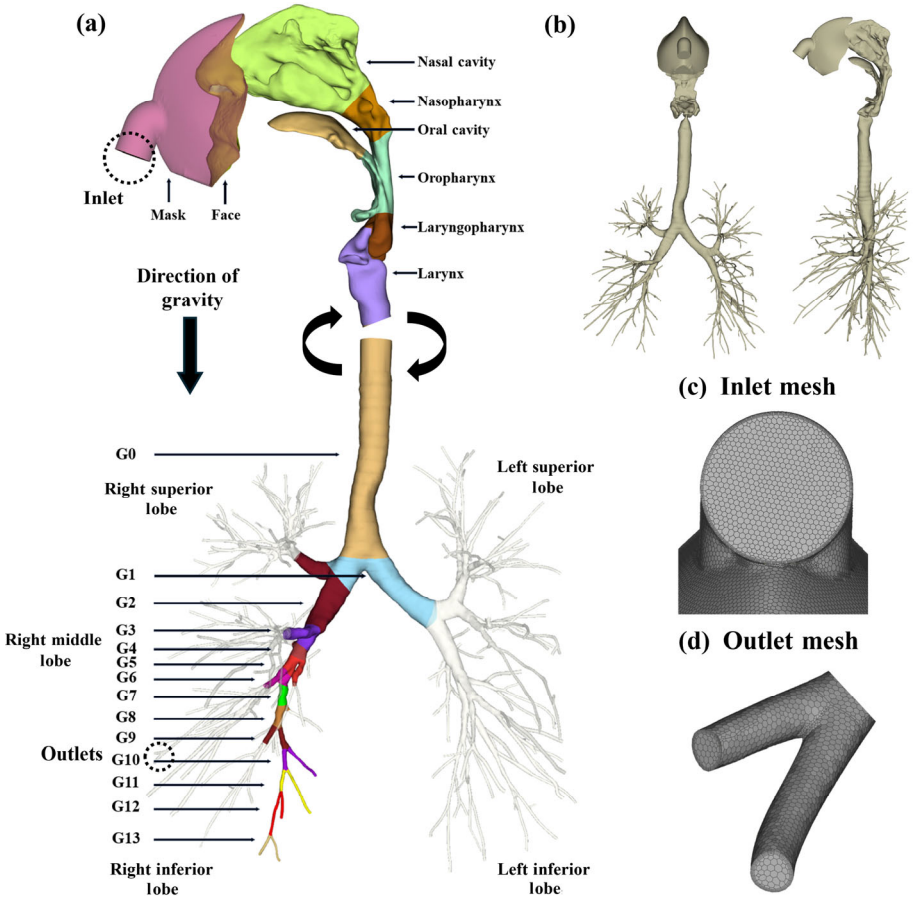

Fig. 1 Visual representations: (a) the computational model of the human respiratory tract developed in the current study; (b) the front and side view of the respiratory tract model of the present study; (c) the polyhedral discretization scheme and the application of a thickness-changing boundary layer at the mask inlet; and (d) similar applications at the outlets of the bronchioles.

turbulence model (ANSYS, 2020a) to accurately simulate inherent turbulence phenomena. The k–ω SST model combines the advantages of both the k–ε and k–ω models, thereby improving the accuracy of predictions in regions characterized by adverse pressure gradients (Menter, 1994), which are critical in the complex geometries of the respiratory tract. The governing equations used in this analysis are enumerated as follows.

Continuity equation:

$$\nabla \cdot u = 0 \tag{1}$$

Momentum equation:

$$\frac{\partial \rho u}{\partial t} + \nabla \cdot (\rho u u) = -\nabla p + \nabla \cdot (\bar{\bar{\tau}}) + \rho g \tag{2}$$

Turbulent kinetic energy equation:

$$\frac{\partial (\rho k)}{\partial t} + \frac{\partial (\rho k u_i)}{\partial x_i} = \frac{\partial}{\partial x_j}\left[\left(\mu + \frac{\mu_t}{\sigma_k}\right)\frac{\partial k}{\partial x_j}\right] + P_k - Y_k + G_b \tag{3}$$

Specific dissipation rate equation:

$$\frac{\partial (\rho \omega)}{\partial t} + \frac{\partial (\rho \omega u_i)}{\partial x_i} = \frac{\partial}{\partial x_j}\left[\left(\mu + \frac{\mu_t}{\sigma_\omega}\right)\frac{\partial \omega}{\partial x_j}\right] + P_\omega - Y_\omega + G_{\omega b} \tag{4}$$

In the SST turbulence model, the eddy viscosity in Eqs. (3) and (4) is formulated as Eq. (5):

$$\mu_t = \frac{\rho k}{\omega}\frac{1}{\max\left[\frac{1}{\alpha^*}, \frac{SF_2}{0.31\omega}\right]} \tag{5}$$

where the damping coefficient α^* in Eq. (5) is given by Eq. (6):

$$\alpha^* = \frac{0.024 + \frac{\rho k}{6\mu\omega}}{1 + \frac{\rho k}{6\mu\omega}} \tag{6}$$

The blending function F_2 in Eq. (5) is defined as Eq. (7):

$$F_2 = \tanh\left(\left(\max\left[2\frac{\sqrt{k}}{0.09\omega y}, \frac{500\mu}{\rho y^2 \omega}\right]\right)^2\right) \tag{7}$$

The turbulence generation due to buoyancy term G_b in Eq. (3) is given by Eq. (8):

$$G_b = -g_i \frac{\mu_t}{\rho Pr_t} \frac{\partial \rho}{\partial x_i} \tag{8}$$

The buoyancy source term $G_{\omega b}$ in Eq. (4) is defined as Eq. (9):

$$G_{\omega b} = \frac{\omega}{k}\left[(1+\alpha)\tanh\left|\frac{v}{u}\right|G_b - G_b\right] \tag{9}$$

where all units, symbols, and constant terms are thoroughly defined in the Nomenclature. The continuity equation (Eq. (1)) ensures mass conservation by equating the mass of air entering and exiting a specific region within the respiratory tract, a critical factor for analyzing respiratory mechanics. The momentum equation (Eq. (2)), based on Newton's second law, provides a mechanism to examine the influence of forces and pressure gradients on airflow, capturing the dynamics between mass flow, pressure, and acceleration. The turbulent kinetic energy (TKE) equation (Eq. (3)) measures the energy associated with the chaotic motion of air particles in turbulent flow, thus quantifying turbulence intensity. The specific dissipation rate equation (Eq. (4)) determines the rate at which TKE dissipates within the flow, shedding light on energy transformations during turbulence. Furthermore, Eqs. (5)–(9) describe various components of the k–ω SST turbulence model, including the calculation of eddy viscosity, damping coefficients, blending functions, and source terms related to buoyancy for both TKE and specific dissipation transport equations.

2.3 Governing equations for the aerosol

The particle motion is modeled using the Euler–Lagrange approach. This approach models the fluid phase as a continuum by solving the Navier–Stokes equations, which describe fluid dynamics. In contrast, the dispersed phase—pharmaceutical aerosols—is modeled by tracking these entities through the flow field. This method allows for detailed interactions between the two phases, enabling the exchange of momentum, mass, and energy. The governing equations used to model the particle motion are listed as follows.

Particle force balance equation:

$$m_p \frac{\partial u_p}{\partial t} = F_{\text{drag}} + F_{\text{gravitation}} \tag{10}$$

The drag force in Eq. (10) is shown in Eq. (11):

$$F_{\text{drag}} = m_p \frac{u - u_p}{\tau_r} \tag{11}$$

where the aerosol relaxation time τ_r (Gosman and Loannides, 1983) in Eq. (11) is given by Eq. (12):

$$\tau_r = \frac{\rho_p d_p^2}{18\mu} \frac{24}{C_D Re} \tag{12}$$

The drag coefficient C_D for spherical aerosols in Eq. (12) is defined as Eq. (13):

$$C_D = a_{1D} + \frac{a_{2D}}{Re} + \frac{a_{3D}}{Re^2} \tag{13}$$

where a_{1D}, a_{2D}, a_{3D} are adjustable over several ranges of Re (Morsi and Alexander, 1972).

The relative Reynolds number Re in Eq. (12) is given by Eq. (14):

$$Re \equiv \frac{\rho d_p \left|\boldsymbol{u}_p - \boldsymbol{u}\right|}{\mu} \tag{14}$$

The gravitational force in Eq. (10) is given by Eq. (15):

$$F_{\text{gravitation}} = m_p g \frac{\rho_p - \rho}{\rho_p} \tag{15}$$

where all units, symbols, and constant terms are thoroughly defined in the Nomenclature. The particle force balance equation (Eq. (10)) embodies the sum of forces acting on aerosol particles within a fluid environment, establishing a relationship between the rate of change in particle velocity and the contributing forces, which include drag (Eq. (11)), gravitational force (Eq. (15)).

2.4 Numerical framework

This study models the complex geometry of the respiratory tract for transient simulation using advanced computational techniques. A polyhedral hybrid mesh with hexagonal prisms in the boundary layers and irregular polyhedral cells in the volume, totaling approximately 7.75 million cells, was employed to capture near-wall fluid dynamics. The mesh design features a changing nodal distance, decreasing from 0.4 mm in the upper airway to 0.2 mm in the smaller bronchial branches, as shown in Figs. 1(c) and 1(d).

Comprehensive details regarding boundary conditions, material properties, and particle configurations are provided in Table 1. The velocity boundary profiles were derived from experimentally determined flow distributions, ensuring accurate velocity magnitude and direction at the boundaries. The velocity at the mask inlet was calculated using the formula: Inlet velocity = Total volume flow rate/Mask inlet area. The instantaneous volume flow rate, as referenced in the formula, was experimentally measured (Nishi, 2004) and incorporated into the CFD model to represent normal (daily activity) breathing conditions (30 breaths per minute,

Table 1 Boundary conditions and material properties of the simulation

Boundary condition	Value	Ref.
Inlet velocity	Velocity profile in Fig. 2(a)	(Nishi, 2004)
Outlet pressure	0 (Pa)	(Saha et al., 2022)
Simulation time	2 (s)	(Nishi, 2004)
Material property		
Air density	1.225 ($kg{\cdot}m^{-3}$)	(ANSYS, 2020b)
Air dynamic viscosity	1.7894×10^{-5} (Pa·s)	(ANSYS, 2020b)
HeliOx density	0.411 ($kg{\cdot}m^{-3}$)	Appendix
HeliOx dynamic viscosity	2.69×10^{-5} (Pa·s)	Appendix
Aerosol density	998.2 ($kg{\cdot}m^{-3}$)	(ANSYS, 2020b)
Volume ratio of helium to oxygen	79:21	—
Particle setting		
DPM tracking scheme	Implicit Euler (low order) and semi-implicit trapezoidal (high order)	(ANSYS, 2020a)
Forces on aerosols	Drag (Eq. (11)), gravity (Eq. (15))	(ANSYS, 2020a)
Wall interaction	Trap	(Longest et al., 2016)
Number of aerosols	100,000	(Kolanjiyil and Kleinstreuer, 2017)
Aerosol diameter	1–100 μm	—
Number of diameters	100	—
Number of aerosols per diameter	1000	—
Aerosol diameter distribution	Rosin–Rammler in Fig. 2(b)	(ANSYS, 2020a)
Drag law for aerosols	Spherical (Eq. (14))	(ANSYS, 2020a)
Release type	Surface release, normal direction	—
Release start time	0.1 (s)	—
Release end time	0.21 (s)	—
Particle time step size	0.001 (s)	—

15 liters per minute) (Wedel et al., 2022), as illustrated in Fig. 2(a). The aerosol diameter distribution by mass was modeled using a two-parameter Rosin–Rammler distribution, with a spread parameter set to 3.5.

2.5 Validation and verification of the CFD model

The numerical methodology utilized in this study has been rigorously validated and verified through extensive evaluations detailed in our prior research, demonstrating robust performance across multiple metrics. The pressure field was systematically assessed by comparing our results with those from earlier numerical studies (Saha et al., 2022). Likewise, the dynamics of mass transfer rates and velocity fields were evaluated in the same respiratory tract model (Huang et al., 2024a, 2024b; Huang and Saha, 2024; Saha et al., 2024b), benchmarking the present results against established numerical and experimental data. A similar approach was applied in the present study, where the total flow percentage across the five lung lobes was calculated and compared to previously reported experimental data and CFD simulation results, as shown in Table 2. The current numerical simulation results fall within the range of prior experimental and numerical findings, validating the accuracy of the mass flow rate for the continuum phase in this study.

To ensure the robustness of our computational model, comprehensive mesh independence tests were conducted in our previous study (Huang et al., 2025b). The mesh independence study was conducted in the same respiratory tract model, testing various mesh density distribution schemes. In addition, a boundary layer independence study was also conducted using polyhedral meshes with 4, 6, and 8 prism layers. The study revealed that variations in the number of prism layers resulted in only negligible differences in both the aerosol deposition patterns and the cross-sectional airflow velocity profiles. These tests confirmed that the respiratory tract achieves mesh independence with a configuration of 7.75 million polyhedral cells and four layers of dynamically changing boundary layer mesh, as depicted in Figs. 1(c) and 1(d).

In the context of particle dynamics, Kolanjiyil and Kleinstreuer (2017) demonstrated that a release rate of 50,000 particles per second is sufficient to achieve particle independence. Accordingly, this study employs a release of 100,000 particles at a rate of 1×10^5 particles per second during inhalation. In addition, this study compared particle deposition efficiency within the nasal cavity to previously reported experimental (Hsu and Chuang, 2012; Kelly et al., 2004) and numerical (Calmet et al., 2019; Schroeter et al., 2011; Shang et al., 2015; Shi et al., 2007) studies, as illustrated in Fig. 3. The normalized particle inertial parameter, a dimensionless quantity, was calculated as Eq. (18):

$$\text{Inertialparameter} = d_p^2 Q \tag{18}$$

The results indicate that the particle deposition efficiency observed in this study aligns well with the range reported in earlier experimental and numerical investigations, exhibiting a similar trend. This consistency validates the discrete phase of the current model.

2.6 Limitation of the model

This study does not incorporate thermal boundary conditions or model the dual-layered airway wall liquids—serum and mucus—and their respective evaporation processes. These

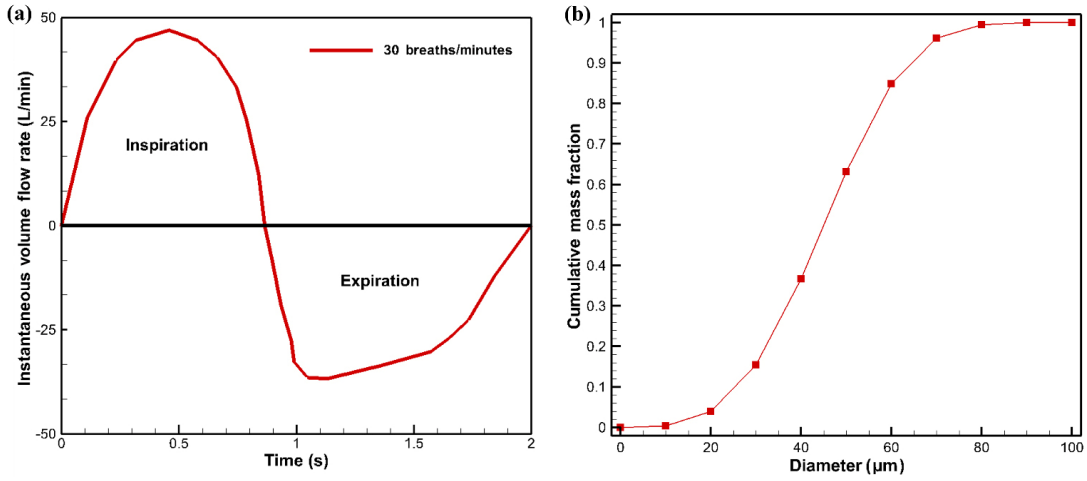

Fig. 2 Realistic boundary conditions: (a) instantaneous volume flow rate during one respiration and (b) aerosol diameter distribution over mass.

Table 2 Validation of simulation results through comparative analysis with previous experimental and numerical data

Total flow (%)	Previous experiment		Previous CFD		Present CFD	
Region	Cohen et al. (1990)	Horsfield et al. (1971)	Islam et al. (2017)	Huang et al. (2024)	Air at time step 0.5 s	HeliOx at time step 0.5 s
Left superior lobe	15.90	20.50	23.38	21.22	21.06	21.63
Left inferior lobe	23.90	24.90	21.82	25.12	25.36	25.78
Right superior lobe	18.20	21.70	21.03	17.60	17.77	17.78
Right middle lobe	9.60	9.60	9.953	11.16	11.10	10.96
Right inferior lobe	32.40	23.20	23.95	24.90	24.72	23.84
Left lung	39.80	45.40	45.20	46.34	46.41	47.41
Right lung	60.20	54.60	54.93	53.66	53.59	52.59

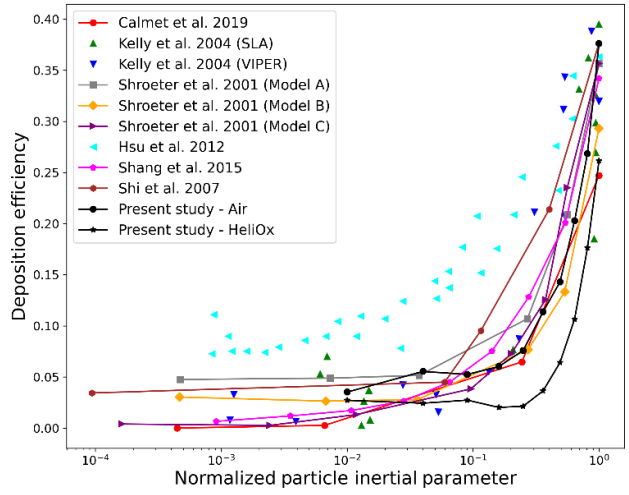

Fig. 3 Particle deposition efficiency within the nasal cavity is validated through comparison with previously reported experimental and numerical data.

exclusions, while simplifying the model, substantially reduce computational complexity and have been determined not to significantly impact the primary focus on airflow and particle dynamics. This streamlined approach is consistent with modeling methodologies employed in both prior and recent research (Gökcan et al., 2024; Gunatilaka et al., 2020; Wedel et al., 2022), emphasizing efficiency and focus in computational simulations.

Another limitation of the present study concerns the recording of particle deposition events during the simulation period. In our computational framework, deposition is recorded at the precise moment a particle makes contact with a wall or exit boundary. While this approach captures the majority of deposition events early in the simulation, a small fraction of particles, typically less than 0.01%, remains in the domain, largely due to entrapment in localized vortices. These residual particles may continue their motion beyond the simulation time frame, potentially leading to additional deposition events that are not accounted for in the current analysis. Future work should consider extending the simulation duration and exploring alternative particle tracking methodologies to fully capture these delayed deposition events and improve the overall assessment of aerosol behavior in the respiratory tract.

A similar limitation arises from the assumption that particles that escape during the inhalation phase do not reenter the airway during exhalation. This simplification was primarily driven by the lack of detailed experimental data on particle recirculation dynamics and the increased complexity that would be associated with modeling such phenomena. Although this assumption may reduce the overall realism of the simulation, its impact is mitigated by the fact that the majority of aerosol particles are deposited in the modeled respiratory tract during inhalation. Nonetheless, future work should strive to incorporate particle re-entrainment during exhalation to capture the full spectrum of aerosol behavior, particularly under cyclic breathing conditions where recirculation might contribute more substantially to overall deposition outcomes.

In addition, the present study employs a simplified representation of the face mask's inlet and outlet mechanisms. Ideally, a longer outlet section would be incorporated to mitigate abrupt gradients at the exit, which could otherwise affect the solution's accuracy. Furthermore, it is important to note that many face masks feature valves for the controlled release of exhaled gases—a characteristic not captured in our current model. Future studies should aim to integrate these components to achieve a more physiologically realistic simulation.

Finally, the present study apply an idealized two-parameter Rosin-Rammler distribution to represent the mass-diameter distribution of aerosol particles. This approach was adopted to facilitate the simultaneous release of particles across a range of diameters in equal numbers, which simplifies data post-processing and allows for straightforward comparisons between different particle sizes. However, in real-world inhalation therapy, the aerosol mass-diameter distribution is highly dependent on the nebulizer device and its operational settings, which can result in significant variability. Consequently, our choice represents an idealized starting point rather than a precise depiction of any specific clinical condition or device. Future studies should aim to incorporate more realistic aerosol generation profiles, potentially informed by empirical data from commercial nebulizers, to improve the translational relevance and accuracy of the simulation outcomes.

3 Results and discussion

The results and discussion of the present research are presented below.

3.1 Deposition patterns in the upper respiratory tract (air vs. HeliOx)

Figure 4 highlights how aerosol deposition patterns differ between breathing ambient air and HeliOx in the upper respiratory tract. In the upper respiratory tract, significant aerosol deposition is observed in the nasal cavity, larynx, and upper trachea when ambient air is used as the carrier gas (Fig. 4(a)). This deposition is particularly prominent for larger particles due to inertial impaction caused by high turbulence in these regions. However, HeliOx shows a reduced deposition in the same regions compared to air (Fig. 4(b)). This is attributed to the lower density and viscosity of HeliOx, which diminishes turbulence and smoothens the airflow.

In the upper respiratory tract, airflow encounters abrupt changes in geometry, such as the nasal cavity's curvature and the narrow laryngeal region, causing turbulence. With air, the higher density and viscosity amplify these turbulent effects, leading to chaotic particle trajectories and increased deposition in the upper regions. HeliOx, being less dense (approximately one-third the density of air), generates lower turbulence levels, allowing particles to pass through these regions with minimal disruption. Larger particles in the 10–100 μm range are particularly susceptible to inertial impaction, where their momentum prevents them from following the airflow's curvature. In the case of HeliOx, the reduced turbulence and steadier flow mitigate the effects of inertial impaction, reducing particle deposition in the nasal cavity and upper airway structures. HeliOx enables smoother flow transitions in the complex geometry of the upper respiratory tract, promoting laminar-like behavior. This minimizes particle collisions with airway walls, in contrast to the chaotic flow associated with air.

Excessive deposition in the upper airways, as observed with air, leads to wasted medication and potential side effects such as irritation in the nasal and laryngeal tissues. By reducing deposition in these regions, HeliOx improves drug delivery efficiency. The ability of HeliOx to reduce upper airway deposition means that a larger fraction of the aerosolized medication reaches the lower airways, where therapeutic effects are often needed (e.g., asthma or COPD treatment). For patients with upper airway sensitivities or conditions such as rhinitis, the smoother flow dynamics of HeliOx minimize irritation and discomfort associated with high turbulence and particle deposition.

The findings align with studies showing that HeliOx significantly reduced deposition in the upper respiratory tract while enhancing transport to deeper lung regions. This reduction can be attributed to the lower density and viscosity of HeliOx, which minimizes turbulence and promotes smoother airflow. The decreased deposition in the upper tract suggests that HeliOx facilitates the passage of aerosols into deeper regions, reducing particle loss in areas such as the nasal cavity and larynx. Previous CFD analyses and experimental observations support the reduced

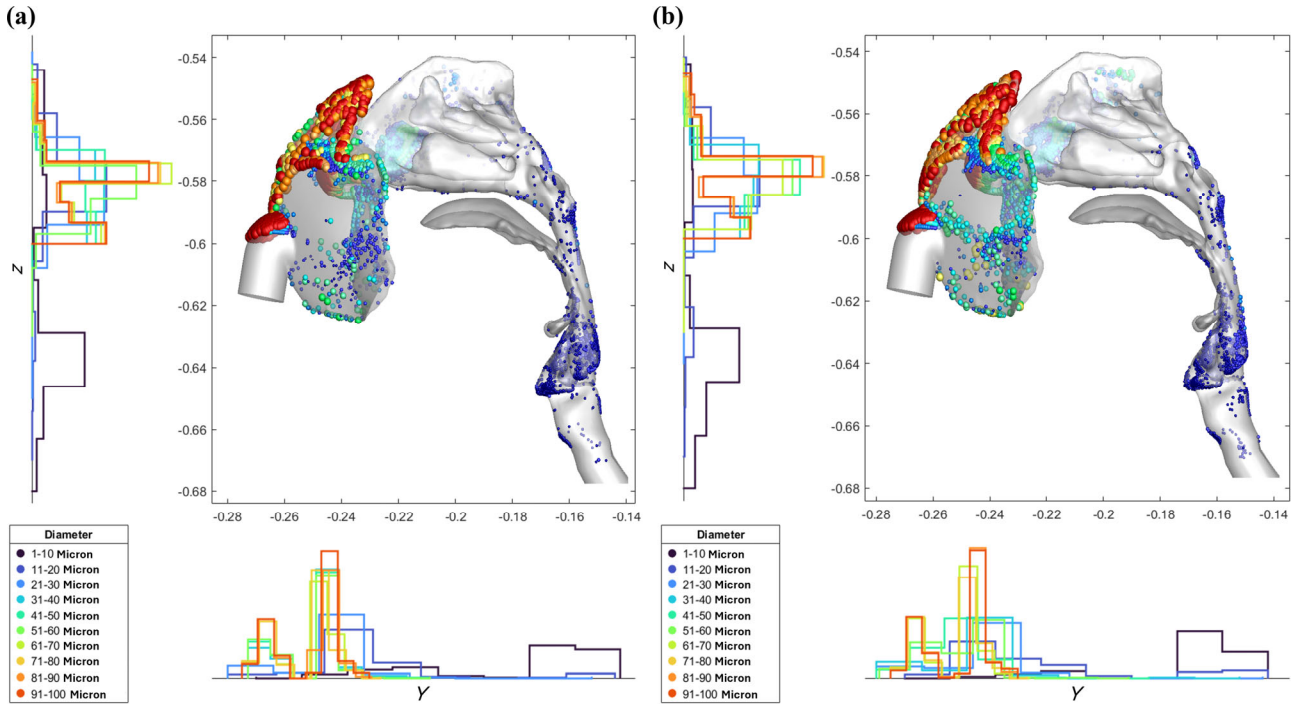

Fig. 4 Deposition pattern of inhaled pharmaceutical aerosols in the upper respiratory tract when breathing (a) air and (b) HeliOx.

turbulence and improved flow characteristics associated with HeliOx. This finding is crucial for improving therapeutic outcomes, particularly in conditions requiring deep lung penetration of aerosolized medications.

3.2 Deposition patterns in the lower respiratory tract (air vs. HeliOx)

Figure 5 illustrates deposition fractions in the lower respiratory tract under the two conditions. With air as the carrier gas, deposition patterns reveal that a significant portion of aerosols is deposited in the mid to upper regions of the lower respiratory tract, with relatively limited penetration into the distal bronchioles and deeper lung regions (Fig. 5(a)). HeliOx, on the other hand, exhibits enhanced aerosol penetration, leading to higher deposition fractions in the distal lung regions (bronchioles and terminal branches). The deposition appears more uniform and extends deeper into the respiratory tract compared to air (Fig. 5(b)). HeliOx enhances deposition in the deeper lung regions, including the bronchioles, compared to air.

The lower density of HeliOx significantly reduces turbulence in the lower airways, allowing particles to follow the streamline flow with less chaotic interaction. This enhances the transport of aerosols to deeper regions. Air, in contrast, creates higher turbulence, which increases deposition in the proximal airways and limits transport to the distal zones. The physical properties of HeliOx (lower density and higher diffusivity) improve particle suspension and minimize inertial effects. This allows both small and medium-sized particles to traverse deeper into the respiratory tree. Air, due to its higher density, results in premature deposition of larger particles in the proximal bronchi due to inertial impaction. Smaller particles (1–10 μm) benefit the most from the reduced turbulence of HeliOx, achieving a higher fraction of deposition in the distal airways and alveolar regions. For larger particles (10–100 μm), HeliOx reduces impaction and gravitational sedimentation effects, resulting in fewer deposits in the mid-airways and a greater likelihood of reaching deeper branches.

The deeper and more uniform deposition achieved with HeliOx ensures that aerosolized medications reach their intended targets in the distal lung regions, where they are most effective for treating conditions such as asthma, COPD, and pulmonary infections. This feature is especially crucial for medications requiring alveolar absorption, such as antibiotics or anti-inflammatory drugs. Conditions such as bronchitis and interstitial lung disease often require precise drug delivery to distal regions. HeliOx facilitates such targeted therapy, improving therapeutic outcomes while reducing drug wastage. By reducing deposition in proximal airways, HeliOx lowers the risk of side effects, such as irritation or inflammation, often caused by medication accumulating in unintended regions of the respiratory tract.

The observed enhancements with HeliOx align with existing research demonstrating its efficacy in improving deposition in distal lung regions. The smoother airflow of

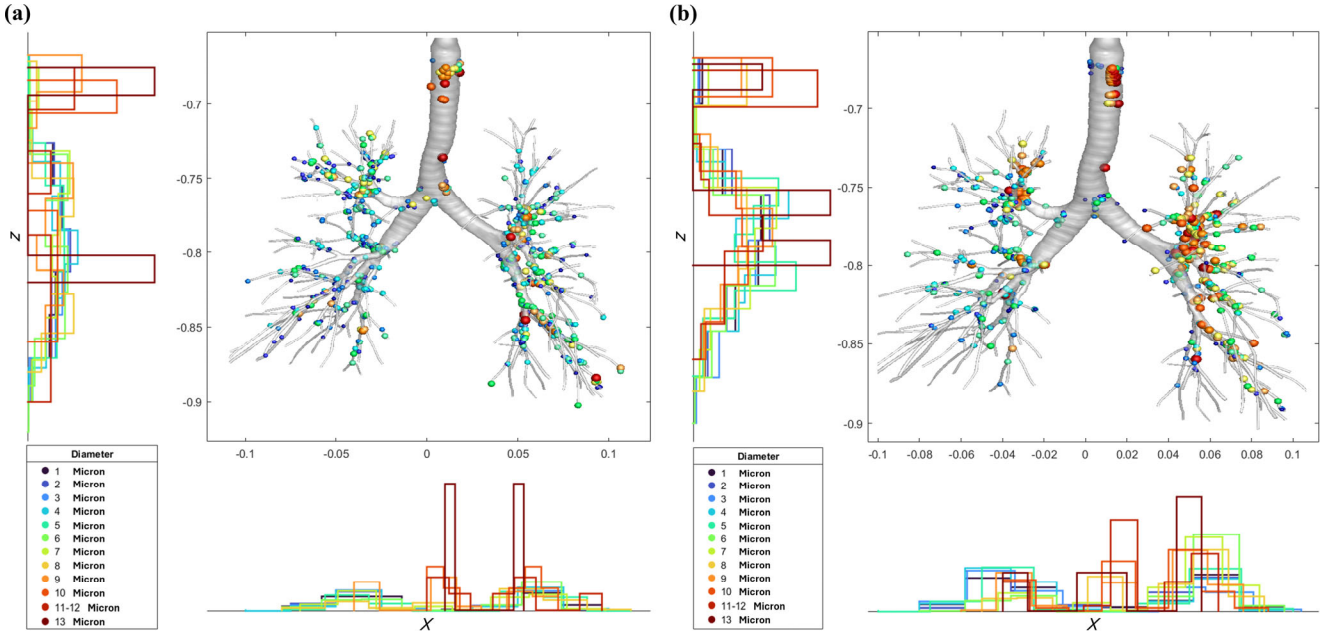

Fig. 5 Deposition pattern of inhaled pharmaceutical aerosols in the lower respiratory tract when breathing (a) air and (b) HeliOx.

HeliOx appears to facilitate aerosol transport to smaller airways. Increased deposition in the lower tract is particularly beneficial for treating diseases such as asthma and COPD, where medication must reach alveolar regions. The findings confirm the potential of HeliOx as an effective carrier gas for pulmonary drug delivery.

3.3 Position fraction heatmap for aerosols (1–100 μm)

The heatmap in Fig. 6 shows the spatial distribution of particles of varying diameters throughout the respiratory tract. Deposition is concentrated in the upper and mid-respiratory tract for larger particles (≥ 10 μm), with limited transport to the distal airways for ambient air as carrier gas. Smaller particles (1–10 μm) show a broader distribution but are still prone to deposition in the mid-airway regions. With HeliOx as a carrier gas, deposition is more evenly distributed, with significantly reduced accumulation in the upper tract and enhanced penetration into deeper regions, particularly for particles in the smaller size range.

With air, larger particles (10–100 μm) experience significant deposition in the upper respiratory tract due to inertial impaction, driven by high turbulence and rapid flow changes. HeliOx reduces turbulence and smooths airflow, allowing larger particles to bypass the upper tract and reach the mid and lower respiratory zones. Smaller particles (1–10 μm) exhibit greater penetration and deeper deposition due to their ability to follow airflow patterns. HeliOx further enhances this effect by minimizing turbulence and enhancing transport efficiency. The smoother flow associated with HeliOx minimizes particle-wall interactions, reducing unwanted deposition in the nasal cavity, larynx, and trachea. Air, with higher turbulence, increases chaotic particle motion, leading to higher deposition rates in proximal regions. For mid-sized particles (10–50 μm), sedimentation due to gravity becomes a dominant deposition mechanism in the mid-airways when using air. HeliOx counteracts this by reducing turbulence and maintaining steadier trajectories. The lower density and viscosity of HeliOx reduce inertial effects for larger particles while also enabling smaller particles to stay suspended longer, resulting in deeper lung penetration and deposition.

The ability of HeliOx to enhance the transport of a wide range of particle sizes is particularly beneficial for therapeutic interventions requiring multisize aerosol formulations. This includes treatments targeting both large airways (e.g., corticosteroids for inflammation) and distal alveolar regions (e.g., antibiotics for infections). The heatmap indicates that HeliOx ensures a more uniform distribution of aerosols, reducing drug wastage in nontarget regions and improving delivery to specific areas of the lung, which is crucial for conditions such as COPD and asthma. By mitigating upper airway deposition, HeliOx minimizes side effects such as irritation or inflammation in the nasal cavity and trachea, commonly observed with conventional air-based aerosol delivery.

Therefore, Fig. 6 demonstrates that HeliOx significantly improves the distribution and transport of aerosols across the respiratory tract for a wide range of particle sizes. By reducing turbulence and minimizing inertial deposition in the upper airways, HeliOx ensures deeper penetration and more uniform deposition. These findings highlight its

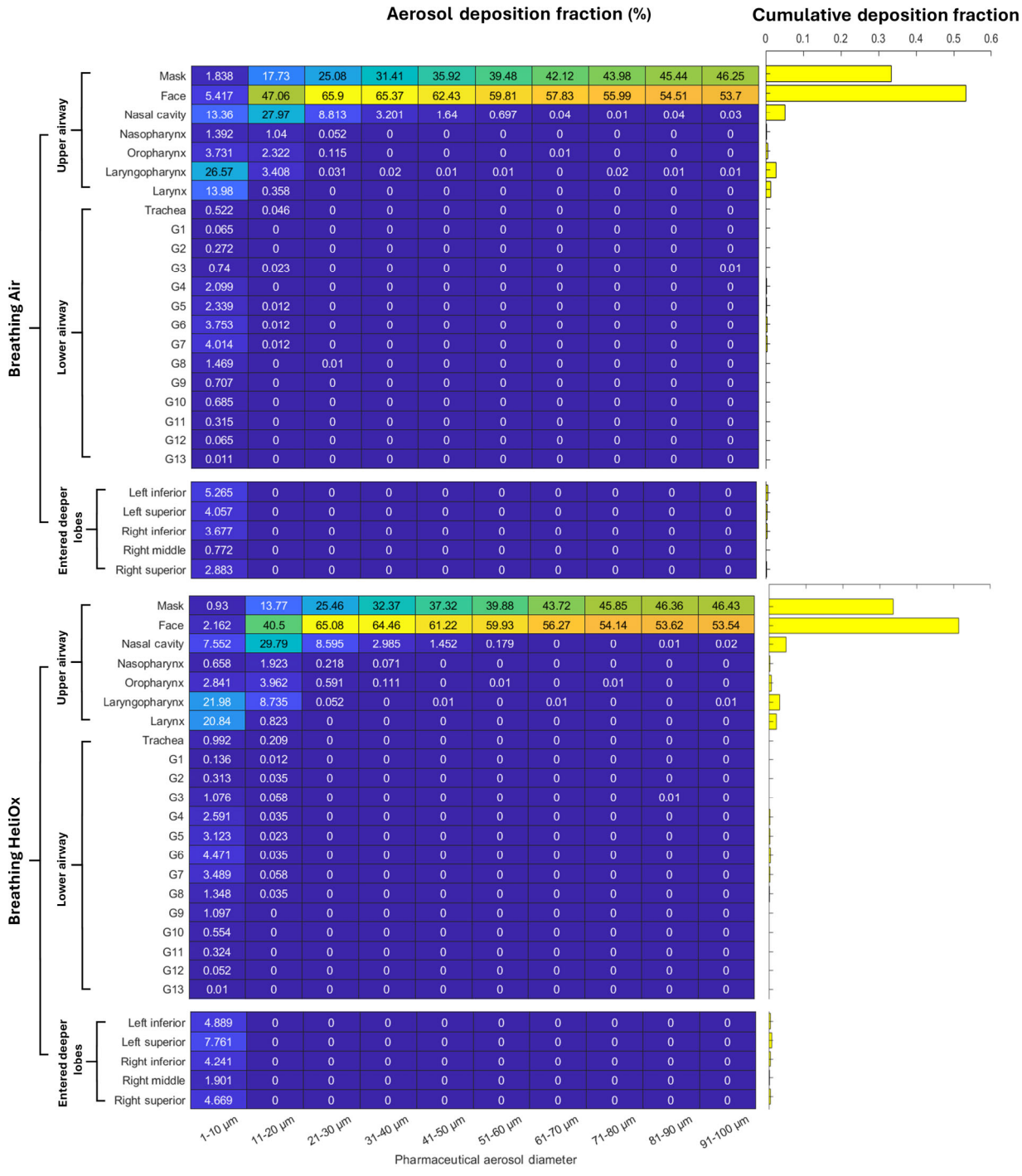

Fig. 6 Position fraction heatmap of aerosols with diameters of 1–100 μm.

potential for optimizing aerosol drug delivery systems and enhancing versatility in aerosol therapy.

3.4 Position fraction heatmap for aerosols (1–10 μm)

Figure 7 zooms in on the distribution of smaller aerosols, which are critical for deep lung deposition. The deposition of small particles is uneven, with concentrations in the mid-respiratory tract and limited penetration into distal lung regions for air as a carrier gas. However, with HeliOx as a carrier gas, aerosols exhibit a broader and more uniform distribution, with significantly higher penetration into the distal airways and alveolar regions.

For air, turbulence-induced eddies and chaotic flow patterns in the upper and mid-respiratory tract reduce the transport efficiency of small particles. The higher density

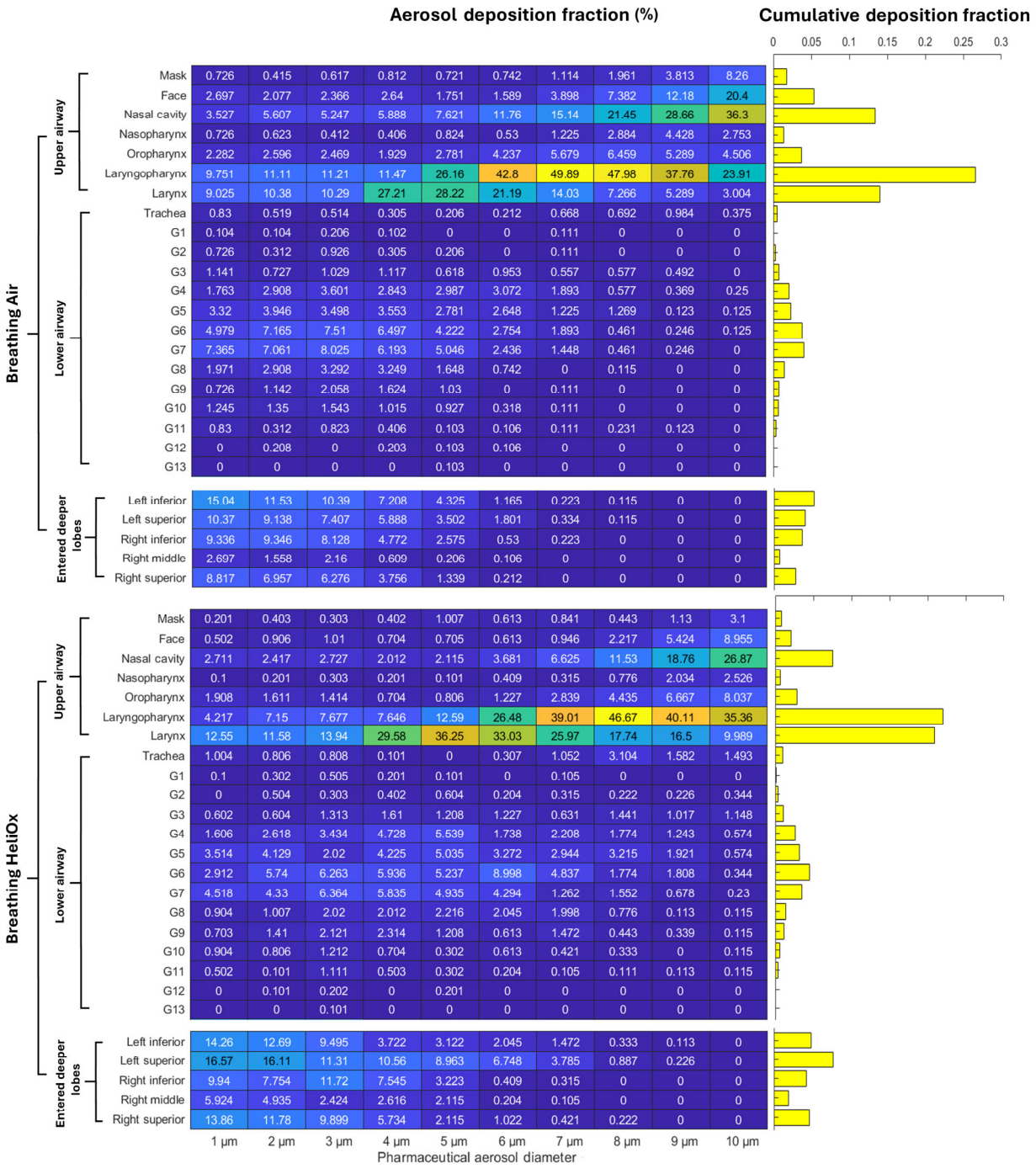

Fig. 7 Position fraction heatmap of aerosols with diameters of 1–10 μm.

of air results in greater drag and lower particle suspension times, limiting distal penetration. For HeliOx, the reduced density of HeliOx minimizes drag on smaller particles, allowing them to remain suspended and follow airflow paths deeper into the respiratory tract. Lower turbulence intensity promotes smoother flow, preventing premature deposition in the upper and mid-respiratory zones. The turbulent kinetic energy associated with air breathing causes chaotic particle motion, leading to increased deposition in unintended areas. HeliOx's lower turbulence levels enable small particles to traverse the airway geometry with minimal interference, enhancing their likelihood of reaching the alveolar region. For particles in the sub-5 μm range, diffusional forces become a dominant factor influencing deposition.

HeliOx, with its higher diffusivity, enhances the random motion of smaller particles, enabling them to reach peripheral regions such as the terminal bronchioles and alveoli. Inertial

and gravitational effects are minimal for particles in the 1–10 μm range, making flow characteristics and turbulence levels the primary determinants of deposition. HeliOx ensures smoother flow trajectories, minimizes particle–wall interactions and further promotes distal transport.

Smaller particles are critical for delivering drugs to alveolar regions, where they can be absorbed into the bloodstream. HeliOx's enhanced transport of these particles makes it particularly effective for treating diseases such as bacterial infections and pulmonary fibrosis. The uniform deposition facilitated by HeliOx minimizes medication wastage and ensures that a higher fraction of the aerosol reaches target regions, improving therapeutic efficacy. By reducing deposition in the mid-respiratory tract, HeliOx minimizes the risk of local drug accumulation, which can cause irritation or inflammation in nontargeted regions.

Overall, Fig. 7 highlights the superior performance of HeliOx in enhancing the transport and deposition of small aerosol particles (1–10 μm) to distal lung regions. Under HeliOx, smaller particles show enhanced penetration into distal regions, with a more uniform distribution. This contrasts with air, where deposition is more concentrated in the upper and mid-respiratory zones. The improved delivery of smaller particles under HeliOx indicates its suitability for therapies targeting alveolar regions. This is especially relevant for conditions requiring deep lung drug delivery, such as bacterial infections or inflammation in alveoli.

Comparing aerosol deposition in air and HeliOx reveals an influence of the carrier gas on particle transport, particularly for smaller aerosols. For micron particles, especially those with larger diameters, inertial impaction remains the dominant deposition mechanism, as evidenced by the immediate deposition on the facemask and in the nasal cavity observed in Fig. 6. However, for aerosols within the 1–10 μm range, although inertial impaction still governs deposition, the turbulence level of the carrier gas exhibits a noticeable effect on particle dispersion. Under HeliOx conditions, where turbulence is moderately reduced compared to normal air, we observed that the deposition hotspot shifts downward within the respiratory tract in Fig. 7. This suggests that the smoother airflow inherent to HeliOx facilitates deeper aerosol penetration, allowing these smaller particles to traverse further into the airway. It is important to emphasize that this shift in deposition is modest, indicating that, while turbulence does contribute to enhanced dispersion, its influence does not overwhelmingly surpass that of inertial forces. Future work employing advanced turbulence models or targeted simulations to isolate the effects of turbulent dispersion would further reveal the relative contributions of these mechanisms under varying respiratory conditions.

3.5 Turbulent kinetic energy during inhalation (air vs. HeliOx)

The contour maps in Fig. 8 display the TKE in the respiratory tract at the 0.5-s mark during inhalation. With air as a

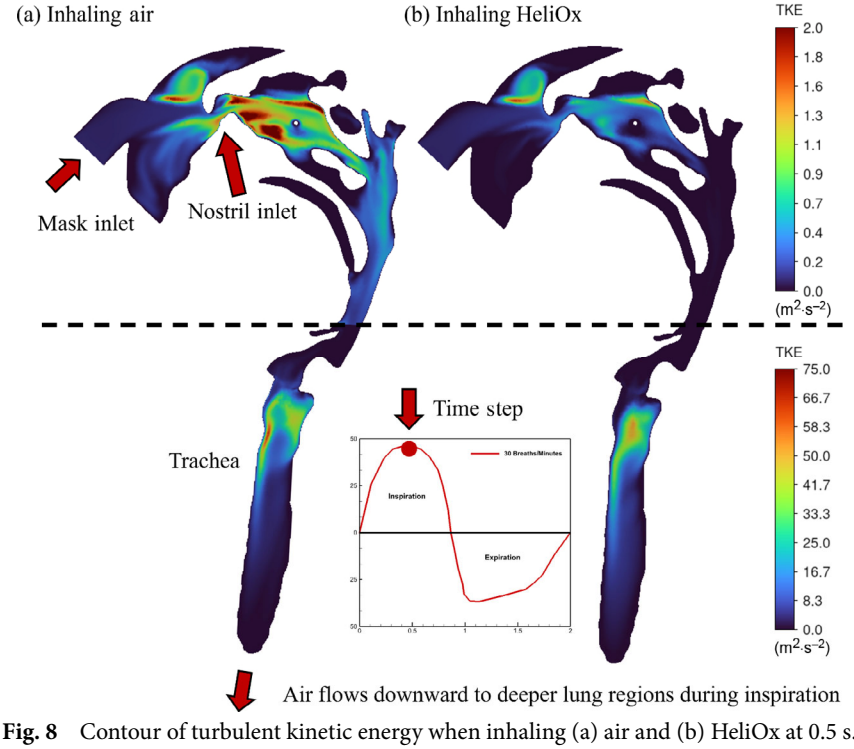

Fig. 8 Contour of turbulent kinetic energy when inhaling (a) air and (b) HeliOx at 0.5 s.

carrier gas, during inhalation, TKE is significantly higher in the upper and mid-respiratory tract, particularly in regions with abrupt geometric changes such as the nasal cavity, larynx, and trachea (Fig. 8(a)). However, with HeliOx as a carrier gas, TKE levels are noticeably reduced throughout the respiratory tract, especially in the upper and mid-airways. The smoother airflow results in less chaotic motion, enabling more laminar-like flow behavior (Fig. 8(b)).

HeliOx has a density of approximately one-third that of air, leading to reduced momentum transfer between fluid and particles. This reduction lowers the generation of turbulence in regions where airflow is constricted or changes direction rapidly. The slightly higher viscosity of HeliOx compared to air enhances its ability to dampen small-scale eddies, further reducing TKE. In the air, sharp bends and narrow regions in the upper respiratory tract, such as the nasal cavity and laryngeal inlet, act as sources of turbulence due to flow separation and recirculation zones. HeliOx mitigates these effects by promoting smoother transitions and minimizing flow instabilities, as evidenced by the lower TKE in these regions. The lower TKE observed with HeliOx results in a more uniform flow profile, reducing velocity gradients that contribute to turbulent energy generation. High TKE associated with air causes chaotic particle motion, leading to increased deposition in nontarget regions such as the upper respiratory tract. The reduced TKE under HeliOx creates a smoother transport pathway, minimizing particle loss in upper regions and enhancing aerosol delivery to the distal airways.

Reduced TKE facilitates the transport of aerosols, particularly smaller particles, to deeper regions of the lungs, enhancing the efficacy of treatments for conditions such as asthma, COPD, and pulmonary infections. By minimizing turbulence, HeliOx reduces the likelihood of particle deposition in nontarget areas, ensuring more efficient drug utilization. Lower turbulence levels result in smoother airflow, which can enhance patient comfort during inhalation therapy, particularly for those with hypersensitive airways or upper respiratory irritation. The ability of HeliOx to suppress turbulence makes it suitable for delivering a variety of aerosolized medications, including corticosteroids, bronchodilators, and antibiotics.

In summary, Fig. 8 demonstrates that HeliOx substantially reduces turbulent kinetic energy during inhalation compared to air, particularly in the upper and mid-respiratory tract. This reduction minimizes turbulence-induced particle deposition and enhances the efficiency of aerosol transport to the distal airways. The findings reinforce the suitability of HeliOx for improving targeted drug delivery, patient comfort, and therapeutic outcomes in pulmonary medicine.

3.6 Turbulent kinetic energy during exhalation (air vs. HeliOx)

Figure 9 examines the TKE patterns during exhalation at the 1-s mark. During exhalation, TKE is prominent in the upper and mid-respiratory tract, especially near the larynx and trachea for air as a carrier gas (Fig. 9(a)). Regions of high turbulence are also observed at branch points where airflow interacts with airway geometry. With HeliOx as a carrier gas, TKE levels are consistently lower across the respiratory tract during exhalation, showing smoother flow profiles compared to air. The reduction in turbulence

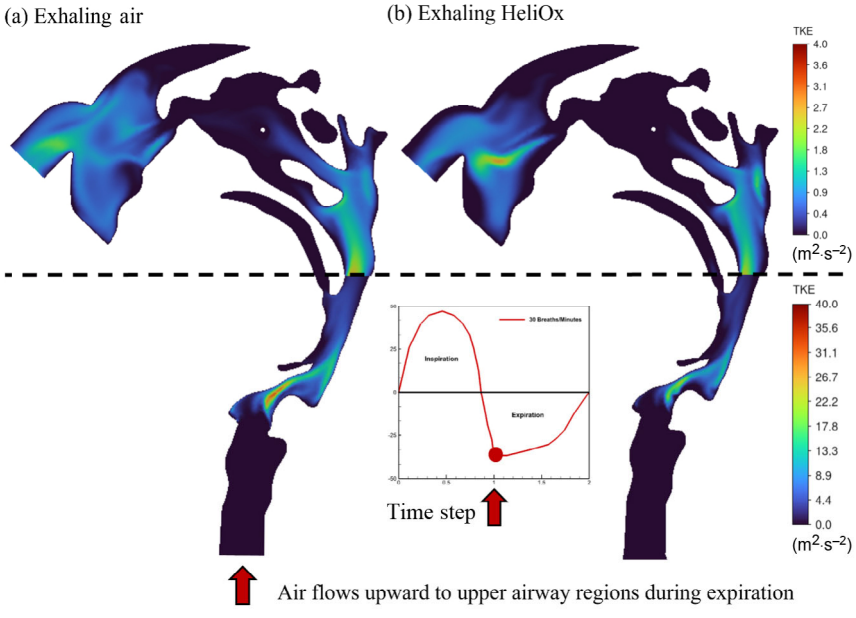

Fig. 9 Contour of turbulent kinetic energy when exhaling (a) air and (b) HeliOx at 1 s.

is particularly noticeable in the nasal cavity, larynx, and trachea (Fig. 9(b)).

The lower density of HeliOx reduces the momentum exchange between air molecules during exhalation, suppressing the formation of turbulent eddies in regions of geometric constriction or branching. Air, being denser, exhibits greater turbulence generation during exhalation due to higher flow resistance and velocity gradients. Exhalation inherently involves airflow against the airway structure's narrowing pathways, amplifying turbulence when using air. HeliOx minimizes these effects by facilitating smoother and more laminar-like flow, maintaining reduced TKE throughout the respiratory tract. The sharp bends and constrictions in the laryngeal and tracheal regions act as sources of turbulence during exhalation. HeliOx, with its smoother flow dynamics, mitigates these turbulence hotspots, as evidenced by the TKE contour. The reduced TKE associated with HeliOx supports efficient clearance of residual aerosol particles during exhalation, preventing particle redeposition in unintended regions, such as the upper respiratory tract.

Lower TKE with HeliOx minimizes the likelihood of residual particles being trapped in the upper airways during exhalation, enhancing the efficiency of drug delivery. This feature is particularly beneficial in therapies requiring high precision, such as in delivering bronchodilators or corticosteroids to targeted regions. The smoother flow dynamics associated with HeliOx reduce turbulence-induced noise and discomfort during exhalation, which is especially advantageous for patients with respiratory hypersensitivity or airway irritation. Conditions such as chronic obstructive pulmonary disease (COPD) and asthma, which often involve airflow limitation and exacerbated turbulence, can benefit significantly from the turbulence-mitigating properties of HeliOx during exhalation.

Figure 9, therefore, demonstrates that HeliOx significantly reduces turbulent kinetic energy during exhalation compared to air, particularly in the upper and mid-respiratory tract. This reduction promotes smoother airflow, enhances aerosol clearance, and reduces the risk of unintended deposition. These findings emphasize the advantages of HeliOx in improving the efficiency and comfort of respiratory therapies, making it a valuable tool in pulmonary medicine for both drug delivery and patient care.

These discussions reinforce the advantage of HeliOx in pulmonary drug delivery, emphasizing its role in reducing turbulence, enhancing particle transport, and optimizing deposition in targeted lung regions. The findings offer a pathway for improving aerosol therapy, particularly for conditions requiring precise and efficient drug delivery to the lower respiratory tract.

4 Conclusions

This study highlights the potential of HeliOx to significantly enhance drug delivery to deeper regions of the respiratory tract. Employing realistic computational models with dynamic breathing profiles provides valuable insights into how HeliOx reduces turbulence and improves aerosol penetration. The key findings and takeaways are as follows:

- HeliOx moderately lowers turbulence during both inhalation and exhalation, enabling smoother airflow and deeper aerosol penetration into the respiratory tract. This improves aerosol drug delivery depth to a small extent, especially in the lower airways.
- For micron particles, especially those with larger diameters, inertial impaction remains the dominant deposition mechanism. However, for aerosols within the 1–10 μm range, although inertial impaction still governs deposition, the turbulence level of the carrier gas exhibits a noticeable effect on aerosol penetration.
- The aerodynamic properties of HeliOx optimize the delivery of small and large particles (1–100 μm), supporting diverse therapeutic applications and reducing drug wastage in nontarget regions.
- By minimizing upper airway deposition and turbulence, HeliOx reduces side effects, enhances patient comfort and is well suited for a broad range of respiratory diseases, from obstructive to alveolar disorders.
- Realistic computational models with dynamic breathing profiles confirmed the efficacy of HeliOx in optimizing aerosol transport, providing a framework for future drug delivery system design and clinical applications.

Future research should explore the transport and deposition patterns of aerosols under varying breathing conditions, such as rapid or slow respiration rates, to determine their impact on the efficacy of aerosol drug delivery. Different breathing patterns can significantly influence airflow dynamics and particle behavior within the respiratory tract, potentially enhancing or hindering the delivery of medication to targeted regions. Moreover, investigating the effect of moisture within the respiratory tract on aerosol particles is crucial. Moisture can alter particle size through hygroscopic growth, affect particle stability, and influence deposition efficiency. Understanding how varying humidity levels and breathing patterns interact to affect aerosol transport could lead to optimized drug delivery strategies and improved therapeutic outcomes for pulmonary diseases.

Appendix Helium–oxygen mixture property calculation

The molecular weight of HeliOx:

$$M_{\mathrm{HeliOx}} = x_{\mathrm{O_2}} \times M_{\mathrm{O_2}} + x_{\mathrm{He}} \times M_{\mathrm{He}} = 0.21 \times 32 + 0.79 \times 4 = 9.88\ \mathrm{g/mol} \quad \text{(A1)}$$

The density of the HeliOx:

$$\rho_{\mathrm{HeliOx}} = \frac{PM_{\mathrm{HeliOx}}}{RT} = \frac{1 \times 9.88}{0.08206 \times 293.15} = 0.411\ \mathrm{g/cm^3} \quad \text{(A2)}$$

Interaction coefficient between oxygen and helium:

$$\Phi_{\mathrm{O_2-He}} = \frac{\left[1 + \sqrt{\frac{\eta_{\mathrm{O_2}}}{\eta_{\mathrm{He}}}}\left(\frac{M_{\mathrm{He}}}{M_{\mathrm{O_2}}}\right)^{0.25}\right]^2}{\sqrt{8\left(1 + \frac{M_{\mathrm{O_2}}}{M_{\mathrm{He}}}\right)}} = \frac{\left[1 + \sqrt{\frac{1.919 \times 10^{-5}}{1.910 \times 10^{-5}}}\left(\frac{4}{32}\right)^{0.25}\right]^2}{\sqrt{8\left(1 + \frac{32}{4}\right)}} = 0.3 \quad \text{(A3)}$$

$$\Phi_{\mathrm{O_2-O_2}} = \frac{\left[1 + \sqrt{\frac{\eta_{\mathrm{O_2}}}{\eta_{\mathrm{O_2}}}}\left(\frac{M_{\mathrm{O_2}}}{M_{\mathrm{O_2}}}\right)^{0.25}\right]^2}{\sqrt{8\left(1 + \frac{M_{\mathrm{O_2}}}{M_{\mathrm{O_2}}}\right)}} = \frac{\left[1 + \sqrt{\frac{1.910 \times 10^{-5}}{1.910 \times 10^{-5}}}\left(\frac{32}{32}\right)^{0.25}\right]^2}{\sqrt{8\left(1 + \frac{32}{32}\right)}} = 1 \quad \text{(A4)}$$

$$\Phi_{\mathrm{He-O_2}} = \frac{\left[1 + \sqrt{\frac{\eta_{\mathrm{He}}}{\eta_{\mathrm{O_2}}}}\left(\frac{M_{\mathrm{O_2}}}{M_{\mathrm{He}}}\right)^{0.25}\right]^2}{\sqrt{8\left(1 + \frac{M_{\mathrm{He}}}{M_{\mathrm{O_2}}}\right)}} = \frac{\left[1 + \sqrt{\frac{1.910 \times 10^{-5}}{1.919 \times 10^{-5}}}\left(\frac{32}{4}\right)^{0.25}\right]^2}{\sqrt{8\left(1 + \frac{4}{32}\right)}} = 2.39 \quad \text{(A5)}$$

$$\Phi_{\mathrm{He-He}} = \frac{\left[1 + \sqrt{\frac{\eta_{\mathrm{He}}}{\eta_{\mathrm{He}}}}\left(\frac{M_{\mathrm{He}}}{M_{\mathrm{He}}}\right)^{0.25}\right]^2}{\sqrt{8\left(1 + \frac{M_{\mathrm{He}}}{M_{\mathrm{He}}}\right)}} = \frac{\left[1 + \sqrt{\frac{1.919 \times 10^{-5}}{1.919 \times 10^{-5}}}\left(\frac{4}{4}\right)^{0.25}\right]^2}{\sqrt{8\left(1 + \frac{4}{4}\right)}} = 1 \quad \text{(A6)}$$

Viscosity of HeliOx:

$$\eta_{\mathrm{HeliOx}} = \sum_{i=1}^{n} \frac{x_i \eta_i}{\sum_{j=1}^{n} x_j \Phi_{ij}} = \frac{0.21 \times 1.919 \times 10^{-5}}{0.21 \times 1 + 0.79 \times 0.3} + \frac{0.79 \times 1.910 \times 10^{-5}}{0.21 \times 2.39 + 0.79 \times 1} = 2.69 \times 10^{-5}\ \mathrm{Pa \cdot s} \quad \text{(A7)}$$

Funding note

Open Access funding enabled and organized by CAUL and its Member Institutions.

Acknowledgements

The authors gratefully acknowledge the computational facilities provided by the University of Technology Sydney (UTS). Furthermore, AI-assisted technology (ChatGPT 4) was employed for language editing and grammar checking to enhance the clarity and coherence of the manuscript. The research contributions of author Xinlei Huang are supported by the China Scholarship Council under Grant ID 202208410137.

Declaration of competing interest

The authors have no competing interests to declare that are relevant to the content of this article.

References

Abd-Elsayed, A., McMaster, M. 2023. Respiratory adjuncts: Heliox, nitric oxide, epoprostenol, and intraoperative steroids. In: *Clinical Science, Advanced Anesthesia Review*. Abd-Elsayed, A., ed. New York: Oxford Academic, 244–C95.S9.

ANSYS. 2020a. ANSYS Fluent Theory Guide. Available at https://ansyshelp.ansys.com/public/account/secured?returnurl=////Views/Secured/corp/v252/en/flu_th/flu_th.html

ANSYS. 2020b. ANSYS Fluent User's Guide. Available at https://ansyshelp.ansys.com/public/account/secured?returnurl=/////Views/Secured/corp/v252/en/flu_ug/flu_ug.html

Barach, A. L. 1935. The use of helium in the treatment of asthma and obstructive lesions in the larynx and trachea. *Annals of Internal Medicine*, 9(6): 739–765.

Calmet, H., Inthavong, K., Eguzkitza, B., Lehmkuhl, O., Houzeaux, G., Vázquez, M. 2019. Nasal sprayed particle deposition in a human nasal cavity under different inhalation conditions. *PLoS One*, 14: e0221330.

Cheng, Y. S. 2014. Mechanisms of pharmaceutical aerosol deposition in the respiratory tract. *AAPS PharmSciTech*, 15: 630–640.

Cohen, B. S., Sussman, R. G., Lippmann, M. 1990. Ultrafine particle deposition in a human tracheobronchial cast. *Aerosol Science and Technology*, 12: 1082–1091.

Corcoran, T. E., Gamard, S. 2004. Development of aerosol drug delivery

with helium oxygen gas mixtures. *Journal of Aerosol Medicine*, 17: 299–309.

Corcoran, T. E., Shortall, B. P., Kim, I. K., Meza, M. P., Chigier, N. 2003. Aerosol drug delivery using heliox and nebulizer reservoirs: Results from an MRI-based pediatric model. *Journal of Aerosol Medicine*, 16: 263–271.

Crowe, C., Sommerfeld, M., Tsuji, Y., Crowe, C. 1998. *Multiphase Flows with Droplets and Particles*. Boca Raton: CRC Press.

Curtis, J. L., Mahlmeister, M., Fink, J. B., Lampe, G., Matthay, M. A., Stulbarg, M. S. 1986. Helium-oxygen gas therapy use and availability for the emergency treatment of inoperable airway obstruction. *Chest*, 90: 455–457.

D'Angelo, E., Santus, P., Civitillo, M. F., Centanni, S., Pecchiari, M. 2009. Expiratory flow-limitation and heliox breathing in resting and exercising COPD patients. *Respiratory Physiology & Neurobiology*, 169: 291–296.

Dailey, P. A., Harwood, R., Walsh, K., Fink, J. B., Thayer, T., Gagnon, G., Ari, A. 2017. Aerosol delivery through adult high flow nasal cannula with heliox and oxygen. *Respiratory Care*, 62: 1186–1192.

Darquenne, C., Prisk, G. K. 2004. Aerosol deposition in the human respiratory tract breathing air and 80:20 heliox. *Journal of Aerosol Medicine*, 17: 278–285.

Dastoorian, F., Pakzad, L., Kozinski, J., Behzadfar, E. 2022. A CFD investigation on the aerosol drug delivery in the mouth–throat airway using a pressurized metered-dose inhaler device. *Processes*, 10: 1230.

Del Puppo, M., Meister, L., Médale, M., Allary, C., Nicollas, R., Moreddu, E. 2023. Heliox simulations for initial management of congenital laryngotracheal stenosis. *Pediatric Pulmonology*, 58: 230–238.

Despas, P. J., Leroux, M., Macklem, P. T. 1972. Site of airway obstruction in asthma as determined by measuring maximal expiratory flow breathing air and a helium-oxygen mixture. *The Journal of Clinical Investigation*, 51: 3235–3243.

Dhand, R., Guntur, V. P. 2008. How best to deliver aerosol medications to mechanically ventilated patients. *Clinics in Chest Medicine*, 29: 277–296.

Dong, J., Shang, Y., Inthavong, K., Chan, H. K., Tu, J. 2017. Numerical comparison of nasal aerosol administration systems for efficient nose-to-brain drug delivery. *Pharmaceutical Research*, 35: 5.

Farooq, U., Riaz, H. H., Munir, A., Zhao M., Tariq, A., Islam, M. S. 2023. Application of heliox for optimized drug delivery through respiratory tract. *Physics of Fluids*, 35: 103321.

Gemci, T., Shortall, B., Allen, G. M., Corcoran, T. E., Chigier, N. 2003. A CFD study of the throat during aerosol drug delivery using heliox and air. *Journal of Aerosol Science*, 34: 1175–1192.

GeomagicWrap. 2022. Geomagic wrap overview. Canonsburg, USA.

Gökcan, M. K., Kurtuluş, D. F., Aypak, A., Köksal, M., Ökten, S. R. 2024. Insights from 3D modeling and fluid dynamics in COVID-19 pneumonia. *Medical & Biological Engineering & Computing*, 62: 621–636.

Gosman, A. D., Ioannides, E. 1983. Aspects of computer simulation of liquid-fueled combustors. *Journal of Energy*, 7: 482–490.

Gunatilaka, C. C., Schuh, A., Higano, N. S., Woods, J. C., Bates, A. J. 2020. The effect of airway motion and breathing phase during imaging on CFD simulations of respiratory airflow. *Computers in Biology and Medicine*, 127: 104099.

Harris, P. D., Barnes, R. 2008. The uses of helium and xenon in current clinical practice. *Anaesthesia*, 63: 284–293.

Hashemian, S. M., Fallahian, F. 2014. The use of heliox in critical care. *International Journal of Critical Illness and Injury Science*, 4: 138–142.

Horsfield, K., Dart, G., Olson, D. E., Filley, G. F., Cumming, G. 1971. Models of the human bronchial tree. *Journal of Applied Physiology*, 31: 207–217.

Hsu, D. J., Chuang, M. H. 2012. *In vivo* measurements of micrometer-sized particle deposition in the nasal cavities of Taiwanese adults. *Aerosol Science and Technology*, 46: 631–638.

Huang X., Clemon, L. M., Islam, M. S., Saha, S. C. 2022. Optimization of fluid characteristics in the main nozzle of an air-jet loom. *Textile Research Journal*, 92: 525–538.

Huang X., Francis, I., Paul, A. R., Saha, S. C. 2025a. Techniques of airway-structure modeling. In: *Biological Flow Modelling*. Boca Raton, USA: CRC Press, 1–28.

Huang, X., Francis, I., Saha, G., Rahman, M. M., Saha, S. C. 2024a. Large eddy simulation-based modeling of cold-air inhalation from nasal cavities to the distal lung: Insights for athlete health and performance. *Results in Engineering*, 23: 102475.

Huang, X., Saha, S. C. 2024. Large eddy simulation of heat and mass transfer in a human respiratory tract in a cold environment. In: Proceedings of the 24th Australasian Fluid Mechanics Conference.

Huang, X., Saha, S. C., Saha, G., Francis, I., Luo, Z. 2024b. Transport and deposition of microplastics and nanoplastics in the human respiratory tract. *Environmental Advances*, 16: 100525.

Huang, X., Yin, Y., Saha, G., Francis, I., Saha, S. C. 2025b. A comprehensive numerical study on the transport and deposition of nasal sprayed pharmaceutical aerosols in a nasal-to-lung respiratory tract model. *Particle & Particle Systems Characterization*, 42: 2400004.

Bleich, H. L., Boro, E. S., Ingram, R. H. Jr., McFadden, E. R. Jr. 1977. Localization and mechanisms of airway responses. *New England Journal of Medicine*, 297: 596–600.

Islam, M. S., Gu, Y., Farkas, A., Paul, G., Saha, S. C. 2020. Helium–oxygen mixture model for particle transport in CT-based upper airways. *International Journal of Environmental Research and Public Health*, 17: 3574.

Islam, M. S., Saha, S. C., Sauret, E., Gemci, T., Gu, Y. T. 2017. Pulmonary aerosol transport and deposition analysis in upper 17 generations of the human respiratory tract. *Journal of Aerosol Science*, 108: 29–43.

Kass, J. E., Castriotta, R. J. 1995. Heliox therapy in acute severe asthma. *Chest*, 107: 757–760.

Kelly, J. T., Asgharian, B., Kimbell, J. S., Wong, B. A. 2004. Particle deposition in human nasal airway replicas manufactured by different methods. Part I: Inertial regime particles. *Aerosol Science and Technology*, 38: 1063–1071.

Khajeh-Hosseini-Dalasm, N., Longest, P. W. 2015. Deposition of particles in the alveolar airways: Inhalation and breath-hold with pharmaceutical aerosols. *Journal of Aerosol Science*, 79: 15–30.

Kleinstreuer, C., Feng, Y., Childress, E. 2014. Drug-targeting methodologies with applications: A review. *World Journal of Clinical Cases*, 2: 742–756.

Kolanjiyil, A. V., Kleinstreuer, C. 2017. Computational analysis of aerosol-dynamics in a human whole-lung airway model. *Journal of Aerosol Science*, 114: 301–316.

Labiris, N. R., Dolovich, M. B. 2003. Pulmonary drug delivery. part I: Physiological factors affecting therapeutic effectiveness of aerosolized medications. *British Journal of Clinical Pharmacology*, 56: 588–599.

Longest, P. W., Tian, G., Khajeh-Hosseini-Dalasm, N., Hindle, M. 2016. Validating whole-airway CFD predictions of DPI aerosol deposition at multiple flow rates. *Journal of Aerosol Medicine and Pulmonary Drug Delivery*, 29: 461–481.

Lu, T. S., Ohmura, A., Wong, K. C., Hodges, M. R. 1976. Helium–oxygen in treatment of upper airway obstruction. *Anesthesiology*, 45: 678–680.

Medical, M. M. 2021. Mimics Medical 24.0 – Instructions for Software Use. Available at https://dagin96kbrjqj.cloudfront.net/etc/med/MIS24-beta/Release%20Notes%20Materialise%20Mimics%20Medical%2024.0%20BETA.PD

Menter, F. R. 1994. Two-equation eddy-viscosity turbulence models for engineering applications. *AIAA Journal*, 32: 1598–1605.

Morsi, S. A., Alexander, A. J. 1972. An investigation of particle trajectories in two-phase flow systems. *Journal of Fluid Mechanics*, 55: 193–208.

Nishi, M. 2004. Breathing of humans and its simulation. LSTM-Erlangen Institute of Fluid Mechanic Friedlich-Alexander-University Erlangen. Available at https://unit.aist.go.jp/ieco/ect/pdf/Nishi_Masterthesis.pdf

Pecchiari, M., Pelucchi, A., D'Angelo, E., Foresi, A., Milic-Emili, J., D'Angelo, E. 2004. Effect of heliox breathing on dynamic hyperinflation in COPD patients. *Chest*, 125: 2075–2082.

Rygg, A., Hindle, M., Longest, P. W. 2016. Absorption and clearance of pharmaceutical aerosols in the human nose: Effects of nasal spray suspension particle size and properties. *Pharmaceutical Research*, 33: 909–921.

Rygg, A., Longest, P. W. 2016. Absorption and clearance of pharmaceutical aerosols in the human nose: Development of a CFD model. *Journal of Aerosol Medicine and Pulmonary Drug Delivery*, 29: 416–431.

Saha, S. C., Francis, I., Huang X., Paul, A. R. 2022. Heat transfer and fluid flow analysis in a realistic 16-generation lung. *Physics of Fluids*, 34: 061906.

Saha, S. C., Francis, I., Saha, G., Huang, X., Molla, M. M. 2024a. Hemodynamic insights into abdominal aortic aneurysms: Bridging the knowledge gap for improved patient care. *Fluids*, 9(2): 50.

Saha, S. C., Huang, X., Francis, I., Saha, G. 2024b. Airway stability in sleep apnea: Assessing continuous positive airway pressure efficiency. *Respiratory Physiology & Neurobiology*, 325: 104265.

Schroeter, J. D., Garcia, G. J. M., Kimbell, J. S. 2011. Effects of surface smoothness on inertial particle deposition in human nasal models. *Journal of Aerosol Science*, 42: 52–63.

Shang, Y. D., Inthavong, K., Tu, J. Y. 2015. Detailed micro-particle deposition patterns in the human nasal cavity influenced by the breathing zone. *Computers & Fluids*, 114: 141–150.

Shi, H., Kleinstreuer, C., Zhang, Z. 2007. Modeling of inertial particle transport and deposition in human nasal cavities with wall roughness. *Journal of Aerosol Science*, 38: 398–419.

Siemens. 2017. NX 12 Release Notes. Available at https://docs.sw.siemens.com/zh-CN/doc/209349590/PL20190529153447339.release_notes

Skrinskas, G. J., Hyland, R. H., Hutcheon, M. A. 1983. Using helium-oxygen mixtures in the management of acute upper airway obstruction. *Canadian Medical Association Journal*, 128: 555–558.

Tian, G., Hindle, M., Longest, P. W. 2014. Targeted lung delivery of nasally administered aerosols. *Aerosol Science and Technology*, 48: 434–449.

Tian, G., Longest, P. W., Su, G., Hindle, M. 2011. Characterization of respiratory drug delivery with enhanced condensational growth using an individual path model of the entire tracheobronchial airways. *Annals of Biomedical Engineering*, 39: 1136–1153.

Vara Almirall, B., Inthavong, K., Bradshaw, K., Singh, N., Johnson, A., Storey, P., Salati, H. 2022. Flow patterns and particle residence times in the oral cavity during inhaled drug delivery. *Pharmaceuticals*, 15: 1259.

Wedel, J., Steinmann, P., Štrakl, M., Hriberšek, M., Cui, Y., Ravnik, J. 2022. Anatomy matters: The role of the subject-specific respiratory tract on aerosol deposition—A CFD study. *Computer Methods in Applied Mechanics and Engineering*, 401: 115372.

Xi, J., Yuan, J. E., Yang, M., Si, X., Zhou, Y., Cheng, Y. S. 2016. Parametric study on mouth–throat geometrical factors on deposition of orally inhaled aerosols. *Journal of Aerosol Science*, 99: 94–106.

Open Access This article is licensed under a Creative Commons Attribution 4.0 International License, which permits use, sharing, adaptation, distribution and reproduction in any medium or format, as long as you give appropriate credit to the original author(s) and the source, provide a link to the Creative Commons license, and indicate if changes were made.

The images or other third party material in this article are included in the article's Creative Commons license, unless indicated otherwise in a credit line to the material. If material is not included in the article's Creative Commons license and your intended use is not permitted by statutory regulation or exceeds the permitted use, you will need to obtain permission directly from the copyright holder.

To view a copy of this license, visit http://creativecommons.org/licenses/by/4.0/.